

## An ultrathin robust polymer membrane for wearable solid-state electrochemical energy storage

Xiang Chu<sup>a,1</sup>, Xun Zhao<sup>b,1</sup>, Yihao Zhou<sup>b</sup>, Yihan Wang<sup>a</sup>, Xueling Han<sup>a</sup>, Yilin Zhou<sup>a</sup>,  
Jingxin Ma<sup>a</sup>, Zixing Wang<sup>a</sup>, Haichao Huang<sup>a</sup>, Zhong Xu<sup>a</sup>, Cheng Yan<sup>a</sup>, Haitao Zhang<sup>a,\*\*</sup>,  
Weiqing Yang<sup>a,\*</sup>, Jun Chen<sup>b,\*\*\*</sup>

<sup>a</sup> Key Laboratory of Advanced Technologies of Materials, Ministry of Education, School of Materials Science and Engineering, Southwest Jiaotong University, Chengdu, 610031, PR China

<sup>b</sup> Department of Bioengineering, University of California, Los Angeles, Los Angeles, CA, 90095, USA

### ARTICLE INFO

#### Keywords:

Wearable bioelectronics  
Solid-state  
Electrochemical energy storage  
Pervasive energy solution  
Personalized healthcare

### ABSTRACT

Developing lightweight, flexible, and foldable electrodes with decent mechanical durability and electrochemical activity is a highly desirable goal for solid-state electrochemical energy storage devices yet remains a formidable challenge to overcome. Herein, we invent a freestanding robust PANI membrane via introducing the dynamic boronate bond to bridge rigid PANI chains with complaint polyvinyl alcohol (PVA) chains. The resultant PANI/PVA membrane (PPM) exhibits remarkable elasticity (17.8% strain) along with excellent tensile strength (33.7 MPa), outperforming the majority of existing state-of-the-art flexible electrochemical PANI membranes. Additionally, the PPM can be further assembled into a wearable solid-state supercapacitor with high electrochemical performance as well as decent mechanical durability. The lightweight, flexible, and foldable PANI membrane represents a great advancement in electrode materials for next-generation wearable solid-state electrochemical energy storage devices.

### 1. Introduction

The Internet of Things (IoT), as a prominent technological revolution of modern society, is transforming our daily lives with unprecedented convenience and intelligence [1–3]. Wearable bioelectronics is one of the key components of IoT devices that enable personalized healthcare as well as interpersonal pervasive communications [4–6]. The number of wearable bioelectronics will increase at an incredibly rate in the near future due to the rapid evolution of fifth generation (5G) wireless communication technologies [7,8]. However, conventional central power supply systems are no longer suitable for sustainably driving billions of distributed wearable bioelectronics [9,10]. Wearable and pervasive power supply is a must for multifarious on-body bioelectronics [11–14]. Solid-state supercapacitors (SSCs) are a promising pervasive energy solution with a collection of compelling features, including high power density, long cycling stability, as well as considerable mechanical

durability [15,16]. To this date, however, it still remains a great challenge for researchers and practitioners to fabricate thin film electrodes for SSCs with both promising electrochemical performance and considerable mechanical performance [17,18].

Numerous materials, such as carbonaceous materials [19], transition metal oxides [20], and conducting polymers (CPs) [21] have been widely investigated to fabricate high performance thin film electrodes for SSCs. Among them, CPs hold unique advantages due to their intrinsic softness and light weight. Moreover, CP electrodes can easily accommodate unpredictable and complicated stress through the movement of segments on polymeric chains [22]. Thus, the mechanical stability of devices can be effectively achieved even when subjected to external stress [23]. Among the wide variety of CPs, polyaniline (PANI) is an outstanding choice due to its low cost, easy fabrication, high thermal stability as well as unique doping/dedoping characteristics [24]. However, the wide-range of adoption of PANI for electrochemical energy

\* Corresponding author.

\*\* Corresponding author.

\*\*\* Corresponding author.

E-mail addresses: [haitaozhang@swjtu.edu.cn](mailto:haitaozhang@swjtu.edu.cn) (H. Zhang), [wqyang@swjtu.edu.cn](mailto:wqyang@swjtu.edu.cn) (W. Yang), [jun.chen@ucla.edu](mailto:jun.chen@ucla.edu) (J. Chen).

<sup>1</sup> These authors contributed equally to this work.

storage is largely shadowed by the poor processability due to its rigid polymeric chain and conjugated backbone structure [25]. Electrochemical deposition and hybridization of PANI with existing films were demonstrated to be two effective methods toward construction of PANI membranes [26,27]. However, electrochemical deposition with more than 150 nm thickness were not solid and compact and thus cannot be free-standing [28]. Similarly, hybridization of PANI with existing films suffers from poor compactness and weak tensile strength due to the existence of multiple interfaces between PANI and the matrix, which hinders their wide applications [25,27]. Therefore, developing PANI membranes into freestanding flexible electrode materials with both promising electrochemical performance and decent mechanical strength is a highly desired goal that still remains a significant challenge.

Here, we report a freestanding and robust PANI membrane fabricated through an efficient supramolecular strategy, in which boronic acid groups are successfully introduced onto PANI polymeric chains through copolymerization of aniline and 3-aminophenylboronic acid (ABA). Compliment polyvinyl alcohol (PVA) chains are simultaneously crosslinked with rigid PANI chains via dynamic boronate bond by adding PVA into a precursor solution containing aniline and ABA. Thus, a freestanding and robust PANI/PVA membrane (PPM) with a delicate crosslinked structure can be effectively achieved via a facile blade coating method. The highly rigid conjugated PANI chains endow the membrane with remarkable mechanical strength, while the compliant PVA chains with softness can provide the membrane with decent flexibility, which exhibits a high tensile strength of 33.7 MPa along with large stretchability (17.8%), outperforming most previously reported freestanding PANI membranes [29–34]. SSCs based on this

electrochemically active membrane deliver a maximum areal capacitance of  $154.4 \text{ mF cm}^{-2}$  as well as high energy density of  $1.91 \text{ mWh cm}^{-3}$  at a power density of  $42.55 \text{ mW cm}^{-3}$ , which is the highest among all the PANI film based wearable SSCs [35–38]. This work paves the way for a scalable and cost-effective approach to developing a lightweight, flexible, and foldable electrode for all solid-state wearable electrochemical energy storage devices, which is expected to make a practical impact in the era of the Internet of things as a pervasive and wearable energy solution.

## 2. Results and discussion

The structural design and fabrication procedure of the freestanding and robust PPM via an effective supramolecular strategy is illustrated in Fig. 1a. Aniline, ABA and PVA were mixed according to a fixed ratio to form the precursor solution. The other solution containing oxidative initiator APS was then added into the precursor solution to trigger the reaction. As the polymerization progresses, PANI (blue chains in Fig. 1a) and PVA (red chains in Fig. 1a) can be effectively crosslinked. In addition, the mixed solution completely loses its fluidity within 6 h due to the thorough polymerization and crosslinking (Fig. S1). To obtain a freestanding PPM, a facile blade coating method is employed to process the mixed solution into a membrane as rapidly as possible, because the mixed solution will lose the vast majority of its fluidity within 10 min. Then the PPM film was peeled off from the glass substrate after thorough rinsing and natural drying. Fig. 1b schematically depicts the molecular structure of this PPM. Hydroxy groups on the PVA chain could react with boronic acid groups on the PANI chain to form dynamic boronate bonds,

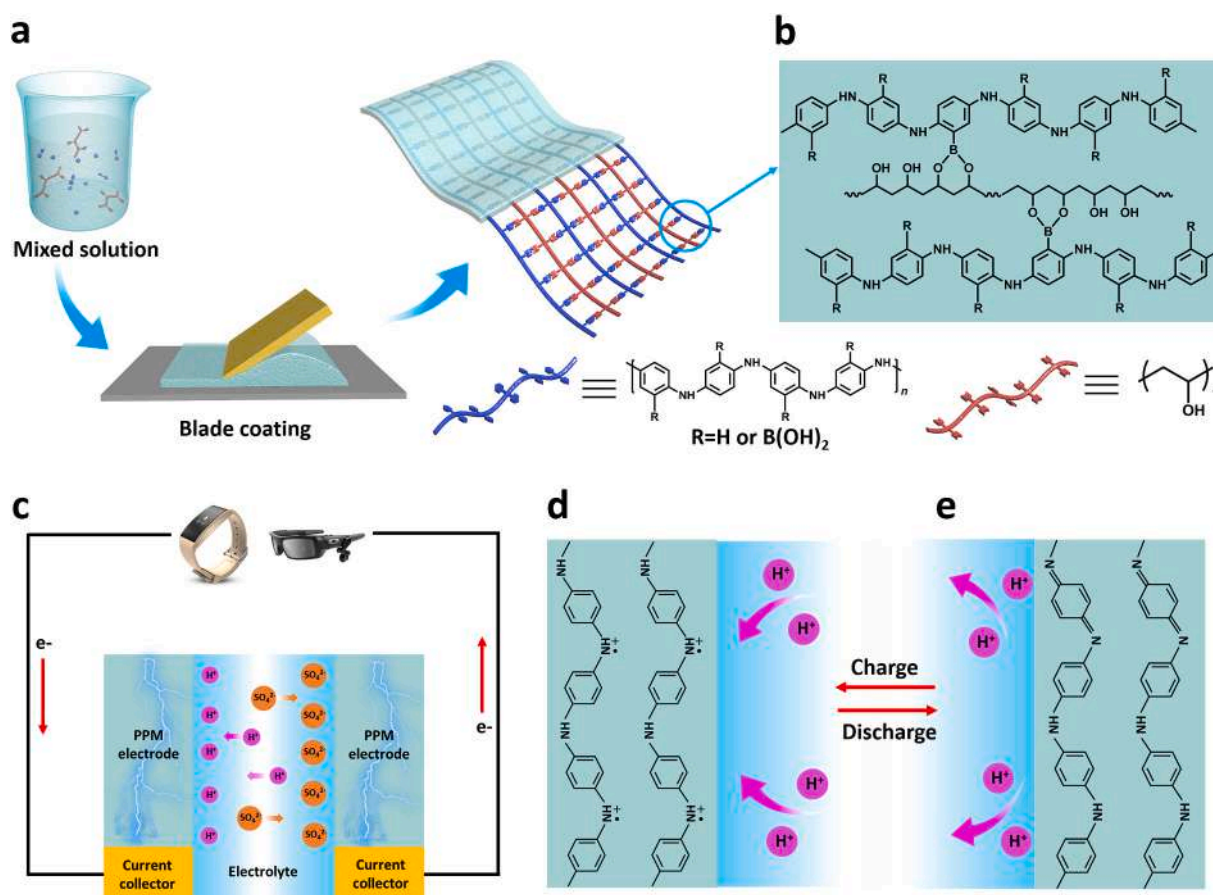


**Fig. 1.** Constructing freestanding and robust polyaniline (PANI) thin membrane using supramolecular strategy. (a) A freestanding PANI/PVA membrane (PPM) is fabricated through the facile blade coating method. (b) Schematic molecular structure of PPM showing the crosslink between rigid PANI chains and compliant PVA chains via dynamic boronate bond. (c) Wearable solid-state supercapacitors (SSCs) are assembled by employing PPM electrodes and gel electrolyte. PANI backbones are (d) doped and (e) de-doped by protons in gel electrolyte during reversible charge/discharge dynamics.

leading to rapid crosslink and gelation. Since the as-prepared PPM is highly freestanding as well as transferable, it could be easily integrated with PVA/H<sub>2</sub>SO<sub>4</sub> gel electrolytes for the fabrication of SSCs (Fig. 1c). During the charge/discharge process, electrochemical active PANI macromolecules can be reversibly doped/dedoped by protons in an electrolyte (Fig. 1d and e). High conductivity and large pseudocapacitance can be consequently achieved.

Digital images of the as-prepared PPM are shown in Fig. 2a. It can be clearly observed that the peeled PPM is highly freestanding and flexible (Fig. 2aI). It can be easily folded into different artistic patterns including triangular and quadrangular stars (Fig. 2aII). Fig. 2a III shows a stainless-steel rod with a radius of 4 mm. It can be helically wrapped by a long, narrow PPM stripe without trackable structural damage, which undoubtedly demonstrates the considerable flexibility of this PPM. The robustness of the PPM is further demonstrated by comfortably hanging a standard 100 g weight on a thin PPM stripe without detectable cracks or breaks (Fig. 2aIV). Moreover, due to the simple preparation process, this PPM can be prepared on a large scale (Fig. 2aV shows large areal flexible PPM with large size of 12 cm × 19 cm), which will give rise to scalable fabrication and commercial applications. To investigate the morphology of this PPM, SEM measurement was employed. Fig. S2a shows the smooth surface of this PPM with some uniform wrinkles, which can be attributed to the volume shrinkage during the natural drying process. According to the AFM characterization (Fig. S2b), the surface roughness of the PPM is ~9 nm, also indicative of the flat and smooth surface of the PPM. Generally, a smooth electrode surface could enable close and dense contact between the electrode and current collector, which further underpins its considerable electrochemical performance. Water contact angle of the PPM is measured to be 65.8° (Fig. S3), indicating a hydrophilic property. Therefore, the PPM is expected to achieve ideal contact with electrolyte and lead to efficient electrode/electrolyte interface. Cross-section SEM images of the PPM with different thicknesses are depicted in Fig. S4. Notably, through adjusting the distance between the stainless-steel blade and glass substrate, the thickness of the PPM can be easily controlled. Obviously, the thickness of PPM prepared by the blade coating method is uniform along the lateral direction. From the cross-sectional view, it can be clearly observed that the PPM

possesses great compactness without trackable porosity or phase interfaces, which contributes to the remarkable mechanical strength of PPM along the direction of elongation due to the fine compatibility of PANI and PVA. Cross-section EDS elementary mapping (Fig. S5) suggests an even distribution of carbon, nitrogen, oxygen and boron on the film, which again confirms the PANI and PVA components are well compatible. It is noteworthy that an even distribution of PANI in freestanding electrode film can enable stable electrochemical performance, which is of great significance for the fabrication of high performance SSCs. However, some methods reported recently such as in-situ polymerization [27] and vapor polymerization [39] are not favorable for the even distribution of PANI on the thin membrane. Because the PANI will preferentially gather on the surface of freestanding membrane, while the inner area of the freestanding membrane usually suffers from low PANI concentration. In this regard, the blade coating coupled supramolecular strategy is superior in fabricating freestanding membranes with uniform PANI distribution.

The PANI in this PPM is doped by strong acid HCl during polymerization. Hence, the PPM has high conductivity in the range of 10<sup>-2</sup> S cm<sup>-1</sup>. As a visualization, the PPM stripe can be directly used as a flexible conductor in circuit containing 4.0 V power supply for powering a green LED bulb (Fig. 2b and Fig. S6). In addition, the stripe can be bent into different shapes such as an arc-shape and S-shape without sacrificing its conductivity. The mechanical performance of the PPM is shown in Fig. 2c. The PPM samples for the tensile strength test were prepared by cutting a large area of PPM into dumbbell shaped stripes (inset in Fig. 2c) through ultraviolet laser beam cutting. It can be clearly observed from the strain-stress curve that the PPM exhibits a remarkable yield strength of 65.6 MPa. After the yielding behavior, an obvious necking phenomenon can be clearly detected, indicating that PANI and PVA are finely compatible through the supramolecular strategy. The PPM stripe was finally broken at an elongation of 17.8% and breaking strength of 33.7 MPa. The considerable mechanical performance of the PPM can be attributed to the delicate molecular design. On one hand, ABA reacts with aniline monomers through cationic polymerization to form rigid conjugated PANI chains, endowing the PPM with high strength. On the other hand, boronic acid groups on ABA molecule can simultaneously

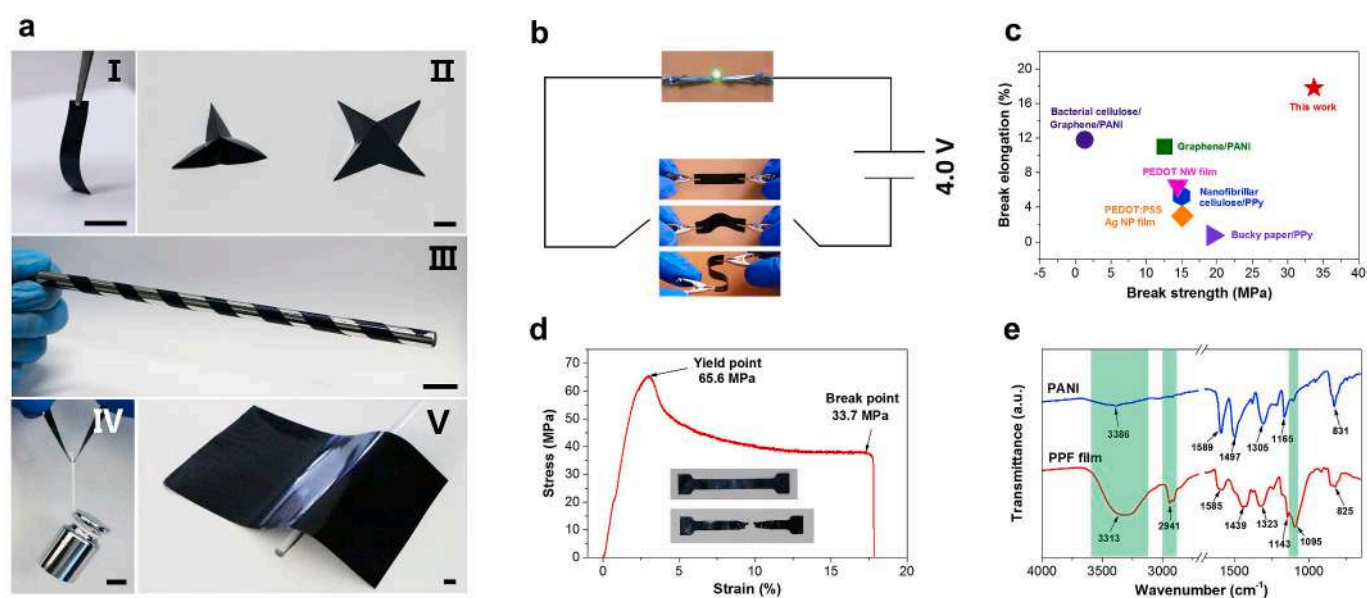


**Fig. 2. Mechanical, electrochemical properties investigation.** (a) (I) The PPM is highly flexible. (II) PPM paper can be folded into various artistic patterns including triangular and quadrangular stars without detectable structural damages. (III) A long, narrow PPM stripe can be densely wrapped onto a stainless steel rod with radius of 4 mm. (IV) A 100 g standard weight can be stably hanged on a narrow PPM stripe. (V) Large areal flexible PPM with large size of 12 cm × 19 cm. The all scale bars in images I-V are 1 cm. (b) PPM stripe under various deformation can be used as a conductor in a circuit for lighting green LED lamp. (c) Stress-strain curve of PPM, inset pictures show dumbbell shaped PPM stripe before and after breaking. (d) Mechanical performance of this PPM outperforms most of the previously reported conducting polymer based freestanding films. (e) FT-IR spectra of PPM.



react with hydroxy groups on PVA to form boronate bonds. The complaint PVA chains provide the PPM with considerable flexibility and elasticity. Consequently, PANI and PVA can be effectively crosslinked and integrated. Therefore, thin membranes featuring both high strength and flexibility is effectively synthesized. Fig. 2d lists the mechanical performance of several state-of-the-art freestanding films based on conducting polymers, including graphene/PANI membrane [29], bacterial cellulose/graphene/PANI membrane [30], PEDOT nanowire membrane [31], nanofibrillar cellulose/PPy membrane [32], PEDOT:PSS/Ag nanoparticles membrane [33], and bucky paper/PPy membrane [34]. Clearly, the PPM outperforms all the afore-mentioned freestanding membranes in both break elongation and break strength. The exact reasons for such an excellent mechanical performance can be explained as follows: i) In this PPM, highly conjugated PANI gives rise to high strength due to the strong  $\pi$ - $\pi$  interaction between PANI chains; while complaint PVA gives rise to high flexibility, leading to large elongation. ii) The two components (PANI and PVA) of this PPM can be effectively bonded through an efficient supramolecular strategy at the molecular level without yielding obvious phase interfaces, which enables its high mechanical performance. In contrast, in many previously reported cases [27,40,41], multiple components were simply hybridized through physical blending. The inevitable interfaces between multiple components undoubtedly lead to poor mechanical performance.

FT-IR spectra of pure PANI and PPM film was shown in Fig. 2e, which can determine the chemical structure of PPM. The pure PANI was synthesized in HCl solution and treated with excess ammonia water in advance to ensure they are in the dedoped state. In the spectrum of pure PANI, the adsorption peaks located at  $1589\text{ cm}^{-1}$  and  $1547\text{ cm}^{-1}$  are assigned to the C=C stretching vibration of the quinoid ring and the benzenoid ring in the PANI backbones, respectively [26]. The characteristic peaks located at  $1305\text{ cm}^{-1}$ ,  $1165\text{ cm}^{-1}$  and  $831\text{ cm}^{-1}$  are attributed to the C-N stretching vibration of secondary aromatic amines, the C=N stretching vibration on quinoid ring ( $\text{-N}=\text{Q}=\text{N-}$ ) and the bending vibration (out of plane) of C-H in the benzene ring, respectively [42]. Additionally, a broad adsorption band at around  $3386\text{ cm}^{-1}$  can be clearly observed in the spectrum of pure PANI, which is associated with the N-H stretching. In the spectrum of the PPM, all of the above-mentioned characteristic peaks of PANI can be obviously detected, undisputedly confirming the existence of PANI in this membrane. Notably, the intensity of the broad peak located at  $3313\text{ cm}^{-1}$  in PPM spectrum is much higher than that of pure PANI. This is due to the existence of dissociative O-H in the PVA chains. Dissociative O-H group generally yield characteristic stretching adsorption peak at around  $3550\text{--}3200\text{ cm}^{-1}$ , which is close to that of N-H on PANI. Thus, the overlapped peak of O-H and N-H appears to be much more intense than that of just N-H [43]. Moreover, two new sharp peaks appeared in PPM spectrum located at  $2941\text{ cm}^{-1}$  and  $1095\text{ cm}^{-1}$ , which can be assigned to the aliphatic C-H stretching and C-O stretching on PVA chains, respectively. This data definitively confirms that PVA and PANI co-exist harmoniously in the PPM. Compared with the spectrum of pure PANI in dedoped state, several peaks in PPM film spectrum red-shift to lower wavenumber ( $1589$  shifts to  $1585\text{ cm}^{-1}$ ,  $1497$  shifts to  $1439\text{ cm}^{-1}$ ,  $1165$  shifts to  $1143\text{ cm}^{-1}$  and  $831$  shifts to  $825\text{ cm}^{-1}$ ). On one hand, this is because the PANI in PPM film is partially doped by HCl during the fabrication process. On the other hand, this can be ascribed to the lower electron density in PANI chains caused by electron-withdrawing group O-H on PVA chains [44]. In the XRD pattern of PPM (Fig. S7), two characteristic peaks located at  $19.7^\circ$  and  $25.2^\circ$  correspond to (0 2 0) and (2 0 0) reflections of PANI, which are in agreement with the FT-IR spectra [24].

To further characterize the chemical composition of the PPM, XPS test was employed. Fig. S8a shows the XPS survey scan of this PPM, in which various elements such as carbon (C1s~284 eV), nitrogen (N1s~399 eV), and oxygen (O1s~532 eV) can be clearly observed. Even the boron (B1s~190 eV) with the low concentration of 1.84% (at. %), can still be traced. The quantitative concentration of each elements was

recorded and is shown in Table S1. Generally, PANI shares a stable C/N ratio of 6 according to its theoretical formula  $(\text{C}_6\text{H}_5\text{N})_n$ . In our sample, the C/N ratio (~11) is much higher than that of pure PANI (6), which is attributed to the existence of PVA chains. The presence of 16.27% oxygen is also aroused from the PVA component. The N1s XPS core level spectrum with binding energy ranging from 397.5 to 404.5 eV is depicted in Fig. S8b. The peaks located at 398.7 eV and 399.4 eV corresponds to quinoid di-imine and benzenoid di-amine, respectively. The peaks above 400 eV (400.1 eV and 401.4 eV) can be attributed to the  $\text{-NH}^+$  nitrogen. According to the peaks area, the  $\text{N}^+/\text{N}$  ratio is calculated to be 49%, indicating a high doping level of PANI polymeric chains [27]. This is consistent with the high conductivity of the PPM ( $1.9 \times 10^{-2}\text{ S cm}^{-1}$ ) tested by standard four-probe apparatus. In the high resolution spectra of C1s XPS core level (Fig. S8c), the C1s core level spectra can be deconvoluted into four peaks: C-C/C-H located at 284.4 eV, C-N/C=N at 285.0 eV, C-N+/C=N+ at 286.0 eV and C-O at 287.9 eV. These results undoubtedly confirm the chemical composition of the as-prepared PPM.

Since this PPM is highly freestanding as well as flexible, it can be easily transferred and tailored for the fabrication of SSCs. As shown in Fig. 3a, a  $100\text{ mm} \times 100\text{ mm}$  PPM was firstly attached closely onto adhesive PET film with the size of  $120\text{ mm} \times 120\text{ mm}$ , serving as the flexible substrate. An ultraviolet laser beam was then used to tailor the PPM into pre-designed interdigital patterns. Gold thin film, serving as the current collector, was sequentially magnetron sputtered onto the interdigitated PPM. Finally, interdigital electrode patterns were wrapped with PVA/ $\text{H}_2\text{SO}_4$  gel electrolyte and PDMS encapsulating materials in sequence to obtain an air-stable wearable device (see details in Experimental Section). Fig. 3b-e shows single SSCs with interdigital, concentric circular, concentric rectangular, and wave-shaped configurations, which further indicates the considerable processability of the PPM during the fabrication process of SSCs. Notably, the interdigital pattern is a widely employed configuration for many in-plane SSCs because this configuration facilitates ion transfer and leads to an efficient electrochemical process [45,46]. Therefore, all the electrochemical tests in this study were conducted with an in-plane interdigital configuration. The detailed size of this interdigital patterns is shown in Fig. S9.

Wearable SSCs are usually used in cases where the accessible volume and area is limited. Therefore, it is always a highly desirable goal for wearable SSCs to deliver as much energy as possible per unit area and volume. In the following discussion of this work, we employ areal capacitance and volumetric capacitance rather than gravimetric capacitance to evaluate the performance of SSCs because these parameters are important considering further commercialization and practical application. First, we investigated the relationship between film thickness and areal capacitance of the device. A series of PPM films with thicknesses spanning from  $9.4\text{ }\mu\text{m}$  to  $62.4\text{ }\mu\text{m}$  were successfully prepared and their corresponding electrochemical performance was then characterized. As shown in Fig. 3f, the areal capacitance increases proportionally with the increase of film thickness. A moderate areal capacitance of  $20.5\text{ mF cm}^{-2}$  was obtained at the film with thickness of  $9.4\text{ }\mu\text{m}$ . When the film thickness increased to  $62.4\text{ }\mu\text{m}$ , a maximum areal capacitance of  $151.9\text{ mF cm}^{-2}$  was delivered (at the current density of  $0.1\text{ mA cm}^{-2}$ ). Fig. 3g depicts areal capacitance of PPM at different current densities ranging from  $0.1\text{ mA cm}^{-2}$  to  $2\text{ mA cm}^{-2}$ . Although thicker films can deliver higher areal capacitance at low current density, the areal capacitance drops rapidly with increasing current density. In detail, areal capacitance of the  $62.4\text{ }\mu\text{m}$  film degrades from  $151.9\text{ mF cm}^{-2}$  to  $61.5\text{ mF cm}^{-2}$  (with just 40.5% retained) when the current density increases by  $20 \times$  (from  $0.1\text{ mA cm}^{-2}$  to  $2\text{ mA cm}^{-2}$ ), indicating its poor rate capability performance. Interestingly, while the current density increases from  $0.1\text{ mA cm}^{-2}$  to  $2\text{ mA cm}^{-2}$ , the thin film ( $9.4\text{ }\mu\text{m}$ ) can maintain 64% of its initial capacitance, suggesting good rate capability. Generally, for a thick film electrode, the electron transfer path is much longer than that of thin film. Then, the redox current cannot be collected effectively by the current collector, especially at large current density.

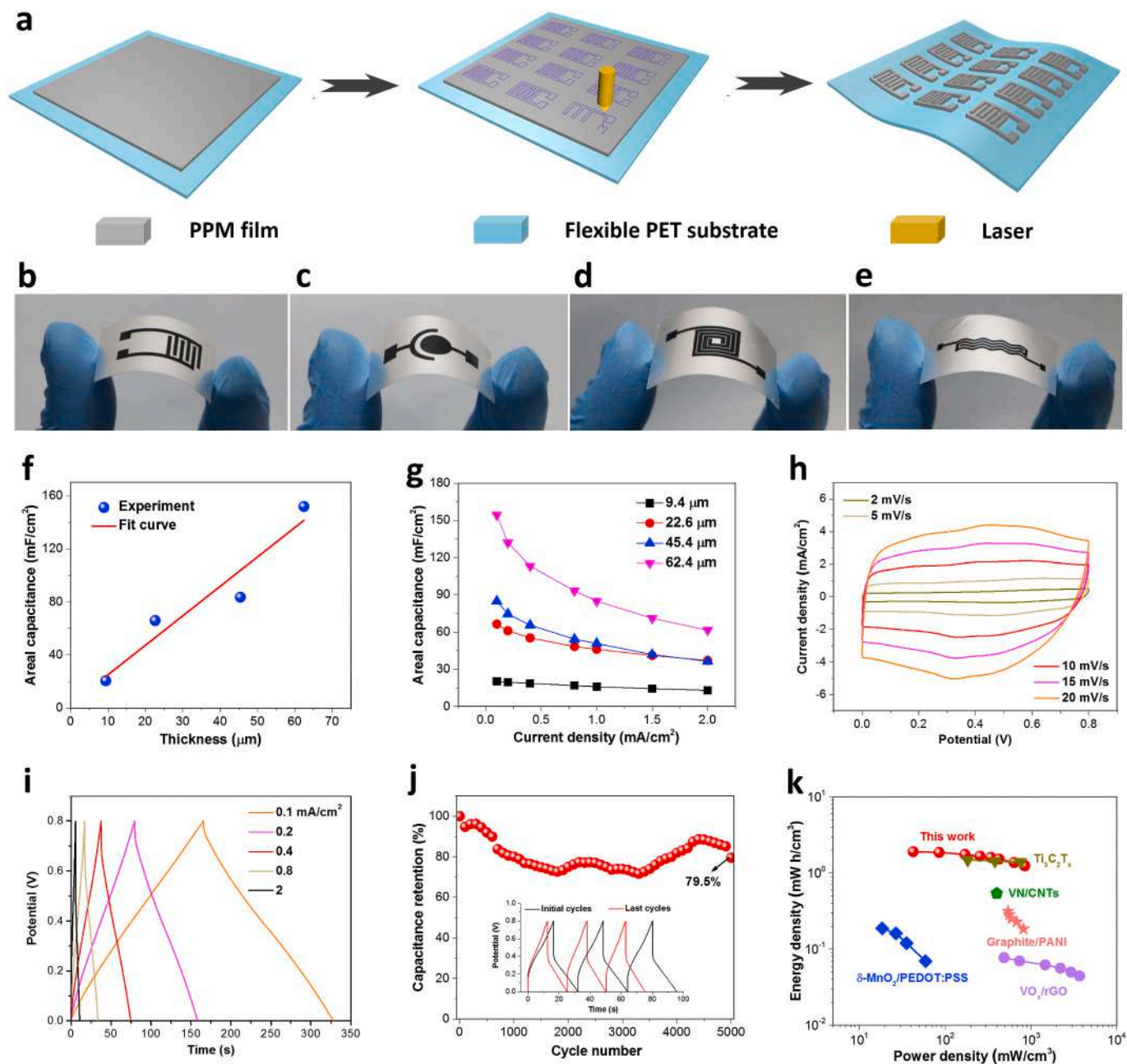


**Fig. 3.** SSCs with high electrochemical performance derived from PPM. (a) Schematic illustration of the fabrication process of coplanar SSCs electrode pattern. SSCs electrode patterns with (b) interdigital, (c) concentric circular, (d) concentric rectangular and (e) wave-shaped configurations. (f) Areal capacitance of SSCs with different membrane thicknesses. (g) Rate performance of SSCs versus increasing current density. (h) CV and (i) GCD curves of  $9.4 \mu\text{m}$  thin membrane-based SSC. (j) Cycling performance of SSC over 5000 GCD cycles, the inset exhibits GCD curves of 1-3rd and 4998-5000th cycles. (k) Ragone plots of SSC and some recently reported supercapacitors based on pseudocapacitive materials.

Consequently, SSCs made from thin film demonstrates a much better rate performance than thick film SSCs.

To further illustrate the electrochemical performance of the PPM, CV and GCD curves of the film with  $9.4 \mu\text{m}$  thickness are shown in Fig. 3h and i. In the CV curves with different scan rates, two couples of characteristic redox peaks of PANI can be clearly observed. When the scan rates increased from  $2 \text{ mV s}^{-1}$  to  $20 \text{ mV s}^{-1}$ , the CV curves can still maintain its shape, indicating good rate capability [47]. Additionally, the CV curves of the wearable SSC remain stable even at bended and twisted states (Fig. S10). This data demonstrates that the SSC can maintain the electrochemical performance while it is subjected to external stress. The GCD curves of PPM exhibit a similar triangle-shape, suggesting good charge-discharge reversibility [48]. The cycling

stability of the SSC was tested for 5000 cycles at a galvanostatic current density of  $2 \text{ mA cm}^{-2}$ . As a result, the SSC demonstrates considerable cycling stability with 79.5% capacitance retained after 5000 GCD cycles (Fig. 3j). The slight increase of capacitance at around 3500-4500th cycles can be attributed to the following reasons: 1) The electrode material generates large volume changes after repeating charging/discharging process and then becomes more open-structured and more accessible to the electrolyte. 2) For a compact PPM, the inner part of bulk membrane could hardly contact with gel electrolyte before cycling. During cycling, the external part of PPM can be fully swollen. Consequently, the inner part becomes more accessible to the gel electrolyte, which leads to an increase in capacitance. Moreover, the IR drop of SSC before and after GCD cycles remains nearly unchanged (see insert of Fig. 3j), indicating

that the ion and charge transfer kinetics maintain relatively stable during long-term cycling. Nyquist plots of wearable SSC with a frequency loop from 100 kHz to 0.1 Hz using a perturbation amplitude of 5 mV is shown in Fig. S11. Equivalent series resistance of the SSC is determined by the intercept of the Nyquist curve with the real axis at high frequencies to be 18.7  $\Omega$ . Due to the high conductivity of the PPM, the areal resistance is calculated to be 11.4  $\Omega \text{ cm}^{-2}$ . Ragone plots of the SSC are depicted in Fig. 3k. The SSC delivers an energy density of 1.91  $\text{mWh cm}^{-3}$  at a power density of 42.55  $\text{mW cm}^{-3}$ . Even at a high-power density of 851.1  $\text{mW cm}^{-3}$ , the energy density is still maintained at 1.25  $\text{mWh cm}^{-3}$ , which is comparable with or even outperforms many state-of-the-art pseudocapacitive materials-based supercapacitors [35–38].

In this study, the SSC prototype shares a stable potential window of 0.8 V with the solid-state PVA/H<sub>2</sub>SO<sub>4</sub> electrolyte. However, this potential window is far away from powering daily consumer electronics. To explore the potential application of SSCs, we further integrated multiple devices in different ways (serial and parallel) and characterized their corresponding electrochemical performance. As for their demonstration, Fig. 4a shows a digital image of large areal flexible SSCs array with multiple SSC units integrated on a flexible substrate, indicating SSCs can be easily integrated through rational design. Fig. 4b shows CV curves of a single SSC and three SSCs tandem circuit at a scan rate of 20  $\text{mV s}^{-1}$ . Obviously, the output potential window can be effectively broadened through tandem connecting. When connected in parallel, the output current is successfully boosted (Fig. 4c) [20]. GCD curves of tandem circuit also demonstrate a higher potential window than that of single device, which is consistent with CV curves (Fig. 4d) [49]. For the three parallel connected SSCs, the stored/released charge is three times higher than that of a single device (Fig. 4e) [50]. Moreover, the tandem circuit was also used to drive daily electronics such as red LED bulb (3.0 V) and liquid crystal display timer (Fig. S12). These encouraging results

clearly demonstrate the potential application of SSCs.

Over the past few years, PANI has been extensively studied in the design and fabrication of supercapacitors in the forms of either pure PANI [48] or PANI composites [51]. Among them, this work holds distinct scientific and technical advancement. The main contributions and innovations of this work can be drawn as following: 1) The PANI and PVA is perfectly crosslinked through dynamic boronate bond without yielding obvious interfaces in this work, the resultant PPM consequently exhibits remarkable mechanical performance that outperforms most previous works. 2) The facile blade coating method gives rise to scalable fabrication of the robust and foldable PPM, which pushes forward the massive production and commercialization of PANI based electrochemical energy storage devices. However, in most previous works, the PANI based materials is not suitable for scalable fabrication due to complicated fabrication procedures. 3) The application potential of this PPM is further demonstrated through assembly of high performance wearable SSCs with PPM electrode. The wearable solid-state electrochemical energy storage device reported in this work will act as an important role in powering the billions of distributed wearable electronics in the upcoming era of Internet of Things.

### 3. Conclusion

Via a supramolecular strategy, a lightweight, flexible, and foldable electrode with decent mechanical strength and electrochemical properties was invented for wearable all solid-state electrochemical energy storage devices. The developed PPM exhibits a breaking strength of 33.7 MPa and elongation of 17.8%, surpassing most existing state-of-the-art conducting polymer-based freestanding films. The assembled SSCs based on PPM deliver a high energy density of 1.91  $\text{mWh cm}^{-3}$  at 42.55  $\text{mW cm}^{-3}$ , large areal capacitance (151.9  $\text{mF cm}^{-2}$ ) as well as remarkable cycling performance (79.5% capacitance retention over 5000

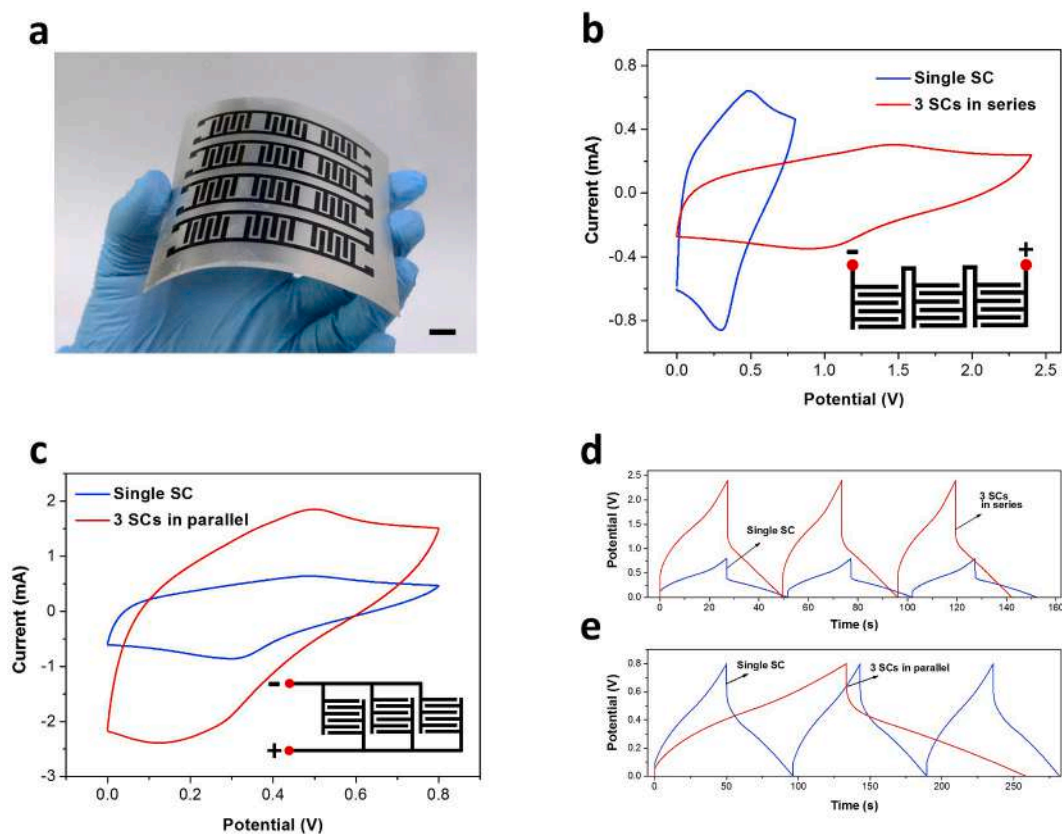


**Fig. 4.** Electrochemical performance of integrated SSCs. (a) Digital image of SSCs electrode array with multiple devices integrated on a flexible substrate, the scale bar is 1 cm. CV curves of SSCs connected (b) in series and (c) in parallel. GCD curves of SSCs connected (d) in series and (e) in parallel.

cycles). This work represents a great advancement in developing light-weight, flexible, and foldable electrodes for the next generation of all solid-state electrochemical energy storage devices.

## 4. Experimental Section

### 4.1. Chemicals and materials

Aniline, 3-aminophenylboronic acid (ABA) monohydrate and polyvinyl alcohol (PVA) with a degree of polymerization of 1799 of analytical grade were purchased from Aladdin. Aniline was distilled under reduced pressure before use. ABA and PVA were used as purchased without further purification. Ammonium persulfate (APS), concentrated HCl, and H<sub>2</sub>SO<sub>4</sub> solution were brought from Chengdu Rongsheng Chemical Reagent Factory, Chengdu, China. Polydimethylsiloxane (PDMS) was purchased from Dow Corning Ltd. (USA) and used as received.

### 4.2. Fabrication of PPM

For a typical fabrication of PPF, solution A was prepared by dissolving 6 mmol APS in 3 mL deionized water. Solution B was prepared by dissolving 4.5 mmol aniline, 0.315 mmol ABA and 9 mL PVA solution (10% wt/wt in DI water) in 2505  $\mu$ L 6 M HCl and 675  $\mu$ L DI water. Both solutions were put into an ice water bath for cooling to 0–4 °C. Then, 2424  $\mu$ L of solution A was added into solution B and mixed quickly by stirring vigorously. After the two solutions were fully blended, the mixed solution was poured onto the glass substrate and blade coated into a thin membrane as rapidly as possible. The PPF will be fully crosslinked and gelled into a solid state in 4–6 h. Then, it was rinsed with adequate deionized water to remove by-products, excess ions, and PVA. Finally, the PPF was naturally dried and peeled off from the glass substrate for further use.

### 4.3. Assembly of SSCs

A large PPM (100 mm  $\times$  100 mm) was first attached densely onto an adhesive PET substrate (120 mm  $\times$  120 mm). An ultraviolet laser beam (UV-3S laser maker, Dazu Ltd., China) was then employed to cut the PPM into a customized interdigital pattern. The power of the ultraviolet laser and cutting times should be optimized to make sure the PPM is fully cut while the PET substrate is not broken. Generally, a PPM with 9.4  $\mu$ m thickness can be fully cut after 13 times with a laser power of 6 W. Sequentially, thin gold film with  $\sim$ 380 nm thickness was magnetron sputtered onto the interdigitated PPM serving as the current collector with a magnetron sputtering equipment (SKY Technology Development Co., Ltd., China) with sputtering power of 40 W for 40 min (working gas of high purity argon). PVA/H<sub>2</sub>SO<sub>4</sub> gel electrolyte was prepared by heating PVA powders (polymerization degree of 1799), concentrated H<sub>2</sub>SO<sub>4</sub>, and deionized water (weight ratio of 1:1:10) mixed solution to 85 °C for 1–2 h until a clear solution was observed. To assemble a SSC, PVA/H<sub>2</sub>SO<sub>4</sub> gel electrolyte was uniformly wrapped onto interdigitated PPM electrode pattern. After that, the encapsulating layer Polydimethylsiloxane (PDMS) was drop casted onto gel electrolyte layer to obtain a sealed device.

### 4.4. Characterization

Scanning Electron Microscope (SEM) tests of PPM were conducted on JSM-7800F Prime (JEOL Ltd.) with an accelerating voltage of 1–5 kV. Energy dispersive spectrometer (EDS) was also conducted in JSM-7800F Prime (JEOL Ltd., Japan) with an Oxford EDS detector at an accelerating voltage of 15 kV and probe current of level 12. Atomic force microscope (AFM) characterization was tested on NanoWizard II (JPK Instruments, Germany) in contact mode. Fourier transformed infrared (FT-IR) spectra with a resolution of 2 cm<sup>-1</sup> were recorded on a Nicolet 6700

spectrometer (Thermo Fisher Scientific, US) from 4000 to 400 cm<sup>-1</sup> at room temperature. Pure PANI sample for FT-IR test was prepared by compressing PANI powders and KBr into a pellet. PPM samples for FT-IR test was prepared by the blade coating method, which is nearly semi-transparent through controlling the thickness of the PPM to a very small value. X-ray diffraction (XRD) of the samples was performed on PANalytical X'Pert Powder diffractometer with Cu K $\alpha$  radiation between 5° and 90°. An X-ray photoelectron spectroscopy (XPS) test was recorded on Thermo Scientific ESCALAB 250Xi.

### 4.5. Performance evaluation

To test the performance of SSCs with PPM electrode, the device was tested with cyclic voltammetry (CV), galvanostatic charge-discharge (GCD), and electrochemical impedance spectroscopy (EIS) methods. The CV characterizations were carried out within the potential window of 0–0.8 V with scan rates ranging from 2–20 mV s<sup>-1</sup>. The GCD measures were carried out within the potential window of 0–0.8 V with current density ranging from 0.1–2 mA cm<sup>-2</sup>. The EIS tests were conducted in the frequency range from 0.01 Hz to 100 kHz with 5 mV ac amplitude. Areal capacitance of the device was calculated from discharge curves according to the following equation:

$$C = It/S\Delta V$$

In this equation,  $I$  (A) is the discharge current,  $t$  (s) is the discharge time,  $S$  (cm<sup>2</sup>) is the area of electrochemical active PPF electrode, and  $\Delta V$  (V) is the voltage interval of discharge. The energy density ( $E$ ) and average power density ( $P$ ) of the flexible solid-state supercapacitors can be expressed as:

$$E = \frac{CU^2}{2V}$$

$$P = \frac{E}{\Delta t}$$

$C$  (F) is capacitance of entire device,  $U$  (V) is cell voltage,  $V$  is effective volume (cm<sup>3</sup>) of electrochemical active materials, and  $\Delta t$  is discharge time.

### Declaration of competing interest

The authors declare that they have no known competing financial interests or personal relationships that could have appeared to influence the work reported in this paper.

### CRediT authorship contribution statement

**Xiang Chu:** Conceptualization, Methodology, Investigation, Formal analysis, Writing - original draft, Visualization. **Xun Zhao:** Conceptualization, Methodology, Writing - original draft, Visualization. **Yihao Zhou:** Methodology. **Yihan Wang:** Methodology. **Xueling Han:** Investigation. **Yilin Zhou:** Investigation. **Jingxin Ma:** Investigation. **Zixing Wang:** Formal analysis. **Haichao Huang:** Formal analysis. **Zhong Xu:** Formal analysis. **Cheng Yan:** Formal analysis. **Haitao Zhang:** Writing - review & editing, Funding acquisition, Supervision. **Weiying Yang:** Writing - review & editing, Funding acquisition, Supervision. **Jun Chen:** Writing - review & editing, Funding acquisition, Supervision.

### Acknowledgements

J. C., W. Y., and H. Z. supervised and guided the whole project. X.C. and X. Z. contributed equally to this work. W. Y. and H. Z. acknowledges the National Natural Science Foundation of China (No. 51977185 and No. 51972277) and Sichuan Science and Technology Program (No. 2018RZ0074). J. C. acknowledges the Henry Samueli School of Engineering & Applied Science and the Department of Bioengineering at



University of California, Los Angeles for the startup support. The authors also would like to express gratitude to Zhangmei Hu, Xiaoke Zheng, Yanzhou Lei, Song Lu and Song Zhang for their help with morphological and structure characterization. Additionally, we really appreciate the support provided by Ceshigo Research Service (<https://www.ceshigo.com/>) for XPS characterization.

## Appendix A. Supplementary data

Supplementary data to this article can be found online at <https://doi.org/10.1016/j.nanoen.2020.105179>.

## References

- [1] G. Chen, Y. Li, M. Bick, J. Chen, *Chem. Rev.* 120 (2020) 3668–3720.
- [2] A.K. Yetisen, J.L. Martinez-Hurtado, B. Ünal, A. Khademhosseini, H. Butt, *Adv. Mater.* 30 (2018) 1706910.
- [3] R. Haight, W. Haensch, D. Friedman, *Science* 353 (2016) 124–125.
- [4] K. Meng, S. Zhao, Y. Zhou, Y. Wu, S. Zhang, Q. He, X. Wang, Z. Zhou, W. Fan, X. Tan, J. Yang, J. Chen, *Matter* 2 (2020) 896–907.
- [5] J. Chen, Y. Huang, N. Zhang, H. Zou, R. Liu, C. Tao, X. Fan, Z.L. Wang, *Nat. Energy* 1 (2016) 16138.
- [6] Z. Zhou, S. Padgett, Z. Cai, G. Conta, Y. Wu, Q. He, S. Zhang, C. Sun, J. Liu, E. Fan, K. Meng, Z. Lin, C. Uy, J. Yang, J. Chen, *Biosens. Bioelectron.* 155 (2020) 112064.
- [7] S. Li, L.D. Xu, S. Zhao, *J. Ind. Inf. Integration* 10 (2018) 1–9.
- [8] Z. Zhou, K. Chen, X. Li, S. Zhang, Y. Wu, Y. Zhou, K. Meng, C. Sun, Q. He, W. Fan, E. Fan, Z. Lin, X. Tan, W. Deng, J. Yang, J. Chen, et al., *Nat. Electron.* 3 (2020) 430.
- [9] L. Atzori, A. Iera, G. Morabito, *Comput. Network.* 54 (2010) 2787–2805.
- [10] C. Yan, Y. Gao, S. Zhao, S. Zhang, Y. Zhou, W. Deng, Z. Li, G. Jiang, L. Jin, G. Tian, T. Yang, X. Chu, D. Xiong, Z. Wang, Y. Li, W. Yang, J. Chen, *Nano Energy* 67 (2020) 104235.
- [11] N. Zhang, F. Huang, S. Zhao, X. Lv, Y. Zhou, S. Xiang, S. Xu, Y. Li, G. Chen, C. Tao, Y. Nie, J. Chen, X. Fan, *Matter* 2 (2020) 1260–1269.
- [12] J. Chen, Z.L. Wang, *Joule* 1 (2017) 480–521.
- [13] Y. Su, J. Wang, B. Wang, T. Yang, B. Yang, G. Xie, Y. Zhou, S. Zhang, H. Tai, Z. Cai, G. Chen, Y. Jiang, L.Q. Chen, J. Chen, *ACS Nano* 14 (2020) 6067–6075.
- [14] Y. Su, T. Yang, X. Zhao, Z. Cai, G. Chen, M. Yao, K. Chen, M. Bick, J. Wang, S. Li, G. Xie, H. Tai, X. Du, Y. Jiang, J. Chen, *Nano Energy* 74 (2020) 104941.
- [15] Y. Wang, Y. Song, Y. Xia, *Chem. Soc. Rev.* 45 (2016) 5925–5950.
- [16] W.B. Fu, E.B. Zhao, X.L. Ren, A. Magasinski, G. Yushin, *Adv. Energy Mater.* 8 (2018) 1703454.
- [17] D.P. Dubal, N.R. Chodankar, D.H. Kim, P. Gomez-Romero, *Chem. Soc. Rev.* 47 (2018) 2065–2129.
- [18] X. Wang, G. Yushin, *Energy Environ. Sci.* 8 (2015) 1889–1904.
- [19] D. Pech, M. Brunet, H. Durou, P. Huang, V. Mochalin, Y. Gogotsi, P.L. Taberna, P. Simon, *Nat. Nanotechnol.* 5 (2010) 651–654.
- [20] Y.-Q. Li, X.-M. Shi, X.-Y. Lang, Z. Wen, J.-C. Li, Q. Jiang, *Adv. Funct. Mater.* 26 (2016) 1830–1839.
- [21] J. Wang, J. Wang, Z. Kong, K. Lv, C. Teng, Y. Zhu, *Adv. Mater.* 29 (2017) 1703044.
- [22] Z. Xu, X. Chu, Y. Wang, H. Zhang, W. Yang, *Chem. Eng. J.* 391 (2020) 123548.
- [23] K. Wang, X. Zhang, X. Sun, Y. Ma, *Sci. China Mater.* 59 (2016) 412–420.
- [24] Y. Xu, M.G. Schwab, A.J. Strudwick, I. Hennig, X. Feng, Z. Wu, K. Müllen, *Adv. Energy Mater.* 3 (2013) 1035–1040.
- [25] H.-P. Cong, X.-C. Ren, P. Wang, S.-H. Yu, *Energy Environ. Sci.* 6 (2013) 1185–1191.
- [26] X. Chu, H. Huang, H. Zhang, H. Zhang, B. Gu, H. Su, F. Liu, Y. Han, Z. Wang, N. Chen, C. Yan, W. Deng, W. Deng, W. Yang, *Electrochim. Acta* 301 (2019) 136–144.
- [27] K. Wang, X. Zhang, C. Li, X. Sun, Q. Meng, Y. Ma, Z. Wei, *Adv. Mater.* 27 (2015) 7451–7457.
- [28] C.M. Carlin, L.J. Kopley, A.J. Bard, *J. Electrochem. Soc.* 132 (1985) 353–359.
- [29] D.W. Wang, F. Li, J.P. Zhao, W.C. Ren, Z.G. Chen, J. Tan, Z.S. Wu, I. Gentle, G. Q. Lu, H.M. Cheng, *ACS Nano* 3 (2009) 1745–1752.
- [30] H. Luo, J. Dong, Y. Zhang, G. Li, R. Guo, G. Zuo, M. Ye, Z. Wang, Z. Yang, Y. Wan, *Chem. Eng. J.* 334 (2018) 1148–1158.
- [31] D. Ni, Y. Chen, H. Song, C. Liu, X. Yang, K. Cai, *J. Mater. Chem.* 7 (2019) 1323–1333.
- [32] C. Sasso, E. Zeno, M. Petit-Conil, D. Chaussy, M.N. Belgacem, S. Tapin-Lingua, D. Beneventi, *Macromol. Mater. Eng.* 295 (2010) 934–941.
- [33] S. Jin, T. Sun, Y. Fan, L. Wang, M. Zhu, J. Yang, W. Jiang, *Polymer* 167 (2019) 102–108.
- [34] J. Che, P. Chen, M.B. Chan-Park, *J. Mater. Chem.* 1 (2013) 4057–4066.
- [35] K. Shen, J. Ding, S. Yang, *Adv. Energy Mater.* 8 (2018) 1800408.
- [36] Y. Wang, Y.-Z. Zhang, D. Dubbink, J.E. ten Elshof, *Nano Energy* 49 (2018) 481–488.
- [37] Q. Jiang, C. Wu, Z. Wang, A.C. Wang, J.-H. He, Z.L. Wang, H.N. Alshareef, *Nano Energy* 45 (2018) 266–272.
- [38] B. Yao, L.Y. Yuan, X. Xiao, J. Zhang, Y.Y. Qi, J. Zhou, J. Zhou, B. Hu, W. Chen, *Nano Energy* 2 (2013) 1071–1078.
- [39] L. Zang, Q. Liu, J. Qiu, C. Yang, C. Wei, C. Liu, L. Lao, *ACS Appl. Mater. Interfaces* 9 (2017) 33941–33947.
- [40] G.P. Hao, F. Hippauf, M. Oschatz, F.M. Wissler, A. Leifert, W. Nickel, N. Mohamed-Noriega, Z.K. Zheng, S. Kaskel, *ACS Nano* 8 (2014) 7138–7146.
- [41] P. Li, Z. Jin, L. Peng, F. Zhao, D. Xiao, Y. Jin, G. Yu, *Adv. Mater.* 30 (2018), e1800124.
- [42] S.A. Chen, H.T. Lee, *Macromolecules* 28 (1995) 2858–2866.
- [43] L.J. Zhang, Y.Z. Long, Z.J. Chen, M.X. Wan, *Adv. Funct. Mater.* 14 (2004) 693–698.
- [44] Y. Wang, Y. Shi, L. Pan, Y. Ding, Y. Zhao, Y. Li, Y. Shi, G. Yu, *Nano Lett.* 15 (2015) 7736–7741.
- [45] Z.S. Wu, K. Parvez, X. Feng, K. Müllen, *Nat. Commun.* 4 (2013) 2487.
- [46] J.J. Yoo, K. Balakrishnan, J. Huang, V. Meunier, B.G. Sumpter, A. Srivastava, M. Conway, A.L. Reddy, J. Yu, R. Vajtai, P.M. Ajayan, *Nano Lett.* 11 (2011) 1423–1427.
- [47] W.W. Li, F.X. Gao, X.Q. Wang, N. Zhang, M.M. Ma, *Angew. Chem. Int. Ed.* 55 (2016) 9196–9201.
- [48] K. Wang, W. Zou, B. Quan, A. Yu, H. Wu, P. Jiang, Z. Wei, *Adv. Energy Mater.* 1 (2011) 1068–1072.
- [49] K. Guo, Y. Wan, N. Yu, L. Hu, T. Zhai, H. Li, *Energy Storage Mater.* 11 (2018) 144–151.
- [50] M. Zhu, Y. Huang, Y. Huang, H. Li, Z. Wang, Z. Pei, Q. Xue, H. Geng, C. Zhi, *Adv. Mater.* 29 (2017) 1605137.
- [51] Y. Wang, X. Yang, L. Qiu, D. Li, *Energy Environ. Sci.* 6 (2013) 477–481.